

ORIGINAL ARTICLE

Interfacing Soft and Hard: A Spring Reinforced Actuator

Hing-Choi Fu,¹ Justin D.L. Ho,¹ Kit-Hang Lee,¹ Yu Cai Hu,¹ Samuel K.W. Au,²
Kyu-Jin Cho,³ Kam Yim Sze,¹ and Ka-Wai Kwok¹

Abstract

Muscular hydrostats have long been a source of inspiration for soft robotic designs. With their inherent compliance, they excel in unpredictable environments and can gently manipulate objects with ease. However, their performance lacks where high force or a fast-dynamic response is needed. In this study, we propose a novel spring reinforced actuator (SRA) that explores the intermediate state between muscular hydrostats and endoskeletal mechanisms. The result is that we dramatically enhance the robot dynamic performance, which is unprecedented in similar kinds of soft robots, while retaining compliant omnidirectional bending. Analytical modeling of the flexible backbone was built and experimentally validated. This is also the first attempt to perform detailed finite element analysis to investigate the strain–stress behavior of the constraining braided bellow tube. The braided interweaving threads are modeled, in which complex thread-to-thread contacts occur. Experimental evaluation of SRAs was performed for actuation force, stiffness, and dynamic response. We showcase the enhanced actuator’s performance in several applications such as locomotion and heavy object manipulation.

Keywords: soft material robotics, bio-inspired robot, fluid-driven actuator, continuum robot

Introduction

MUSCULAR HYDROSTATS HAVE long been an inspiration source in the field of soft robotics. The tentacles of the cephalopod, an elephant trunk,¹ and the human tongue² all come under this class of biological structure. These structures have no underlying endoskeleton and consist entirely of muscles, which make them flexible and conformable, yet dexterous manipulators.

Researchers originally sought to mimic these unique properties using silicone-bodied soft robots driven by specialized fluidic channels.³ Many studies were successful in imitating these muscular hydrostats,⁴ producing safe and compliant robots⁵ that could be used in a range of fields like surgery⁶ and search and rescue.⁷ Through these designs and studies, it became apparent that soft robots share very similar working principles with muscular hydrostats.⁸ Neither have rigid definite structures; and both consist of multiple unidirectional mechanisms that, in concert, perform a range of desired movements.⁹ In nature, these individual mechanisms

are muscles that contract and shorten, whereas in most soft robots, they are fluidic chambers that elongate and expand with increased pressure or volume.¹⁰ However, for hydrostats and soft robots alike, the combination of these individual mechanisms provides a versatile platform for interacting with the environment, enabling actions such as elongation, shortening, bending,¹¹ and twisting.¹²

Current soft robots, like muscular hydrostats, can provide versatile changes to their morphology, in thanks to their soft bodies and fluidic actuation. Their compliance enables gentle manipulation of unknown or delicate objects without needing complex force-feedback control schemes.¹³ Soft robots excel in environments where flexibility and adaptability are essential, but their performance lacks where high force or a fast-dynamic response is needed, ultimately limiting their usage in a range of tasks.¹⁴ As a result, a number of studies have aimed to enhance the performance of soft robots, with some that modify the stiffness characteristics of soft continuum robots by: changing the body materials,¹⁵ optimizing the geometrical features,¹⁶ or varying the braid angle of fiber

¹Department of Mechanical Engineering, The University of Hong Kong, Hong Kong, China.

²Department of Mechanical and Automation Engineering, The Chinese University of Hong Kong, Hong Kong, China.

³Department of Mechanical and Aerospace Engineering, Seoul National University, Seoul, Korea.

constraints.¹⁷ Although these modifications can be integrated into existing designs in a straightforward manner, their influence on robot dynamics is limited, in part, by the range of available materials. In addition, the use of stiffer elastomers tends to reduce their allowable elongation, which can hinder the dexterity of the manipulators.¹⁸

Jamming is an alternative approach commonly used to modulate the stiffness of soft robots.^{19,20} It relies on interlocking forces between granules or material layers induced by a pressure differential. Initially, these granules are able to move freely, allowing unrestricted movement of the soft robot,²¹ but when negative pressure is applied, a “solid-like” state is induced due to intergranular friction and locking forces, which can lead to substantial increases in stiffness.²²

However, several limitations still exist with granular jamming: it cannot be used to increase the actuation force; the nonlinear behavior of the interparticle friction makes the jammed robot dynamics much harder to predict, as it cannot be modeled as linear spring-like behavior²³; and the robot cannot be manipulated while jammed. Moreover, hysteresis due to granule dislocation in the jammed state can adversely affect the control accuracy and dynamic response of the system, especially after prolonged use.²² Although other methods of jamming such as layer jamming^{24,25} aimed to minimize the footprint and nonlinear behavior that jamming mechanisms have, using interleaving film shaped as scales instead of granules, other limitations seen in the granular jamming approach still remained.

A unique approach to augmenting soft robot performance is through the use of hybrid mechanisms. Hybrid actuators integrate rigid components with soft structures to modify their actuation characteristics (Fig. 1). One study proposed a soft actuator design inspired by crustaceans, using a hard exoskeleton with soft actuators inside them.²⁶ Short rigid plates could be mounted at different points along the length of the body to alter the bending profile. The exoskeleton could linearize the force and bending behavior and was easily config-

urable, although the addition of external rigid components may not be ideal for fragile environments and limits the bending to one direction. In a similar manner, *ArthroBots*²⁷ took inspiration from the legs of insects and spiders. They used thin, lightweight rigid links actuated by inflatable balloon joints in combination with antagonistic tendons to allow passive retraction. Although its low mass and compliant joints allowed safe interaction with humans, the slow actuation speed precludes its usage in scenarios requiring a fast response.

Natividad *et al.*²⁸ explored the use of external inflatable fabric balloons combined to actuate an external flexible plastic spine. The design allowed reconfigurability of the bending profile by replacing individual balloons; however, the mechanism was hindered by a slow response time and unidirectional bending. Heung *et al.*²⁹ designed a robotic glove for patients with impaired hand movement that incorporates stiff torque-compensating plates and antagonistic spring components to aid finger extension. Analytical modeling and validation of the bending behavior were undertaken with a focus on kinematics, which were tailored to the single-direction bending of human fingers.

To our knowledge, no previous studies have proposed a suitable enhancement to soft robotic designs that addresses our primary concerns: (i) high output force, (ii) fast dynamic response, and (iii) low hysteresis, while also retaining compliance and dexterous, omnidirectional bending. Therefore, we sought a solution to these problems that many current designs encounter.

In this study, we propose a reinforcement scheme capable of combining soft and rigid properties by incorporation of a flexible spring backbone. The backbone can provide an internal support to the soft robot body and still allow a high degree of bending. Augmenting soft actuators with a passive antagonistic mechanism improves stiffness and response time.³⁰ Furthermore, the restoring force of helical springs has also been shown to reduce hysteresis and to simplify the continuum robot dynamics model to beam mechanics-based

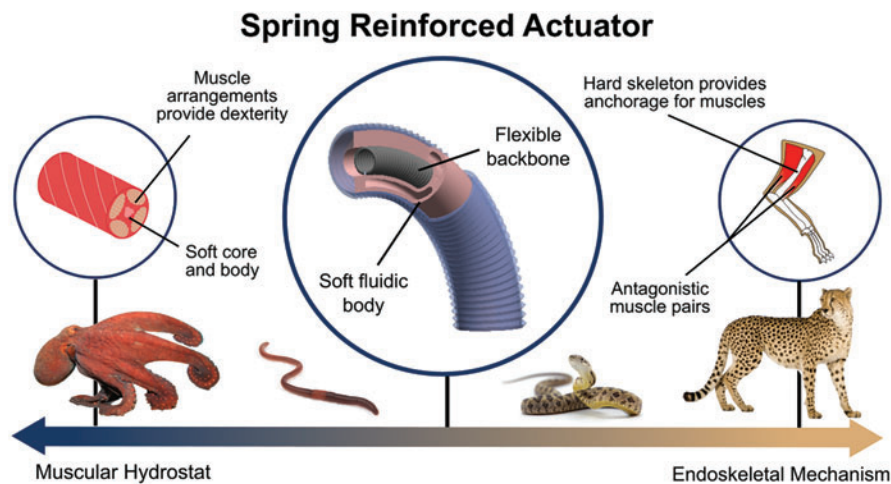


FIG. 1. Conceptual illustration of the proposed actuator. The actuator design is derived from the features of both muscular hydrostats and endoskeletal mechanisms. The octopus and worm (*left*) make use of muscular hydrostatic mechanisms for locomotion and manipulation. They are inherently soft, flexible, and maneuverable, but lack rapid and powerful movements. On the other hand, the snake and cheetah (*right*) can achieve this with their hard-skeletal system. When imagined as a spectrum between these two biological mechanisms, the proposed SRA explores the intermediate state, possessing a hard, yet flexible backbone and a soft fluidic body, providing both power and dexterity. SRA, spring reinforced actuator. Color images are available online.

models.²³ For hyperelastic soft robots, the study on the integration of springs has rarely been carried out. This may be due to various inherent problems that arise when integrating a spring backbone into a soft structure, which we aim to address in this study.

The proposed hybrid actuator consists of a closed-coil spring integrated into the central lumen of a three-chamber soft actuator. A closed-coil spring is used instead of the more common open-coil spring due to its precompression characteristic, which minimizes gaps between coil windings. We analytically characterize the transverse bending behavior of a closed-coil spring and investigate its effect after integration with the soft actuator. A series of experiments evaluated the significantly improved force and dynamic response of the actuator, and a range of applications are presented. The primary contributions of this work are:

- Design and fabrication of a robust spring-reinforced soft actuator with rapid dynamic response and high force output that retains the original continuum bending behavior.
- Analytical modeling and validation of the transverse bending behavior of closed-coil springs and finite element analysis (FEA) of bellow sheaths.
- Experimental evaluation of the spring reinforcement in terms of active actuation force, stiffness, and dynamic performance, namely through step response and bode plot analysis.
- Demonstration of the enhanced soft robotic performance, for example, in heavy object manipulation and locomotion, which is unprecedented in similar kinds and sizes of bending actuator.

Methods

Bioinspiration and implementation

In soft robots, underdamping is a commonly seen characteristic due to the exclusion of stiff or rigid components. From a dynamical point of view, underdamping is characterized by significant overshoot and a long settling time. This causes soft robots to oscillate significantly when a large or abrupt actuation input is provided. Their nonrigid structure exacerbates the effect of self-weight, and force output is limited by buckling of the actuation chambers or perforation of the body.

In nature, we can see a similar trend. Hydrostatic animals often exhibit peristaltic locomotion³¹ and are rarely seen in situations where a high force output or fast movement is needed. Bones in limbs, on the other hand, provide a stiff component that muscles and ligaments can anchor to and enhance the ability for antagonistic muscle pairs to stiffen and provide rapid motion.³² For two muscles to have an antagonistic relationship, the action of one muscle must oppose the action of the other.³³ One example is the human arm in which the bicep flexes the arm and the tricep extends it. When both muscles contract in unison,³⁴ compression of the joint occurs, resulting in enhanced stability and stiffness, which benefits both fine motor manipulation and heavy loading.³³

As a result, an observation is that most animals on both land and water that exert fast and large forces possess an underlying stiff skeleton, like bone or cartilage. By learning from these biological trends seen in nature, we aimed to

combine the strengths seen in vertebrate animals with the maneuverable and compliant nature of muscular hydrostats.

To achieve this, the proposed actuator consists of a soft body combined with a flexible skeleton (Fig. 2a). The soft body is inspired by muscular hydrostats, providing compliant omnidirectional bending using fluidic chambers. For the backbone, a closed-coil spring is integrated into the actuator, providing a definite structure while also providing an antagonistic force against the actuation direction. By selecting a spring as the backbone element, we aimed to improve the rapid dynamic response and force output, while retaining the excellent conformability and manipulability of soft robots.

Design of soft actuator body. The soft body of the actuator is molded from silicone into a cylindrical shape consisting of three equally spaced fluidic chambers (Fig. 2c). A braided sleeve is wrapped around the outer layer of the soft body,³⁵ restricting its radial expansion. Note that the braided sleeve is compressed and folded axially, forming a bellow sheath (Fig. 2b) that tightly encloses the soft body, without hindering its bending motion. The bellow-shaped constraint layer provides a uniform and dense fiber reinforcement compared to helically wound constraints³⁶ and provides a high elongation ratio. When the fluidic chambers are pressurized, their axial expansion produces a bending or elongation motion. With different combinations of pressures in three chambers, the actuator can achieve omnidirectional movement along a conical surface.³⁷

Design of flexible skeleton. Springs are a basic and common component of a mechanical system, allowing a wide selection of materials, dimensions, and precompression. In previous studies, helical metallic springs have demonstrated excellent flexibility and back-drivability when incorporated with cable-driven continuum robots.³⁸ Open-coiled springs (like those seen in car suspension) are often used as the backbone of continuum robots, which can attain effective bending and shortening when pulled by cables.³⁹ However, open-coil springs are not favorable for soft-bodied actuators due to the large gaps between adjacent coils, which can cause local ballooning during inflation, ultimately resulting in premature bursting.⁴⁰

In this study, a closed-coil spring or so-called tension spring is selected as the backbone element as opposed to its open-coiled counterpart. Closed-coil springs can achieve a comparable amount of bending curvature to that of open-coil springs while having much smaller intercoil gaps. They also possess a precompression that is superimposed with the linear elastic force seen in normal springs, providing a bilinear force-displacement behavior. Physically, the spring does not open until the prestress force is overcome. This behavior can be observed in our four-point spring bending tests.

By integrating a closed-coil spring into our actuator design, the precompression gives rise to a significant antagonistic restoring force that can passively enhance the dynamic response of the soft continuum robot. Moreover, the centrally-placed spring can sustain the high compressive force produced inwardly by the inflated soft actuator body, allowing critical components like sensors, cables, or tubes to pass through it freely. In our study, a range of closed-coil tension springs made of spring steel (GB/T 1222-2007) are used to reinforce the soft continuum actuators.

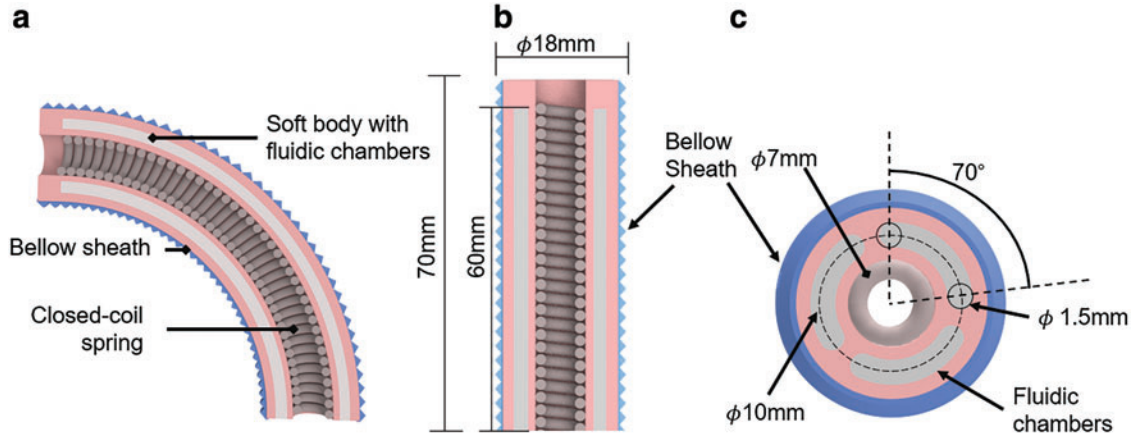


FIG. 2. (a) CAD/CAM overview of the presented SRA during bending, showing three major components of the actuator: the soft body, bellow sheath, and closed-coil spring placed along the actuator's central axis. The bellow sheath restricts radial expansion during chamber inflation, but still allows elongation to permit bending. (b) Side cross-section view of uninflated actuator. The actuator stiffness is greatly increased with the closed-coil spring integrated into the middle channel. Such stiffness can also be modulated based on the properties of the integrated spring. (c) Axial cross section of the actuator. The chambers are designed as a curved slot shape to maximize cross-sectional coverage and to reduce stress concentrations, thus withstanding higher pressures. Color images are available online.

Actuator fabrication

The fabrication process consists of four major steps as follows: (1) molding of the soft body; (2) attachment of the crimped sheath; (3) insertion of the closed coil spring; and (4) encapsulation of the entire system.

The soft body of the hybrid actuator is of tentacle-inspired design, with three parallel fluidic chambers spaced 120° apart that allow omnidirectional bending.³⁵ The soft body was molded with silicone (Dragon Skin 20, Ecoflex; Smooth-On, Inc.) in a three-dimensional (3D) printed mold. In addition to the three fluidic chambers, a central channel was left to allow integration of the spring reinforcement. To enable pneumatic transmission, silicone tubes were connected to the proximal end of each fluidic chamber. A bellow sheath was slipped onto the soft body to limit radial expansion but not the axial elongation of the body (Fig. 3b). The bellow sheath in combination with the spring reinforcement allows the actuator to be inflated to a pressure up to 8 bar.

Afterward, the closed-coil spring with outer diameter matching the inner channel diameter was cut to a suitable length (~ 70 mm) and then inserted into the center channel of the soft body. To fix the spring backbone into place, top and bottom caps were 3D printed (Objet Connex 500; Stratasys) and mounted to the exposed spring ends. Each cap possesses a groove to accommodate the spring during adhesion. The soft actuator was then pulled and elongated to the length of the springs and was fixed to the end caps together with the spring end as shown in Figure 3c.

Modeling of actuator

Modeling of mesh. To allow for large elongation, and hence bending of the actuator, a folded braided tube is used as a constraint on the outer soft body. Although this method has been previously applied to soft robots,^{35,41} detailed studies or simulations are seldom conducted for this kind of folded fiber constraint. An FEA model is thus constructed to simulate the behavior of the mesh. Nomenclature is listed in Table 1.

Geometrical features of the braided tube. The braided tube with mean radius R_o is formed by interweaving of 32 nylon threads of thread radius r_t . The interwoven threads follow the shapes of clockwise (right-handed) and anticlockwise (left-handed) helices about the z -axis, as seen in Figure 4a. The transverse plane of the braided tube in which thread-to-thread contact occurs is shown in Figure 4b. The radial positions of the clockwise “c” and anticlockwise “a” threads are:

$$\begin{aligned} R_c(\alpha) &= R_o + \sqrt{2}rt \cos\left(8\alpha + \frac{\pi}{4}\right), \\ R_a(\alpha) &= R_o - \sqrt{2}rt \cos\left(8\alpha - \frac{\pi}{4}\right) \end{aligned} \quad (1)$$

as indicated in the figure by the curves in green and purple, respectively. In the equation, α is the angular polar coordinate of the point along the tube length and R_o is the initial tube radius.

With H denoting the pitch of the helices, the Cartesian coordinates for the k -th clockwise and the k -th anticlockwise threads where $k=0, 1, \dots, 15$ are:

$$\begin{aligned} \mathbf{X}_k^c &= \begin{bmatrix} R_c\left(\alpha + \frac{k\pi}{8}\right) \cos\left(\alpha + \frac{k\pi}{8}\right) \\ -R_c\left(\alpha + \frac{k\pi}{8}\right) \sin\left(\alpha + \frac{k\pi}{8}\right) \\ \frac{H\alpha}{2\pi} \end{bmatrix}, \\ \mathbf{X}_k^a &= \begin{bmatrix} R_a\left(\alpha + \frac{k\pi}{8}\right) \cos\left(\alpha + \frac{k\pi}{8}\right) \\ R_a\left(\alpha + \frac{k\pi}{8}\right) \sin\left(\alpha + \frac{k\pi}{8}\right) \\ \frac{H\alpha}{2\pi} \end{bmatrix} \end{aligned} \quad (2)$$

with $0 \leq \alpha \leq \alpha_{\text{top}}$ where α_{top} is determined by the initial length of the entire tube, and H is the helical pitch of the threads.

For the presented tube, $R_o = 5.1$ mm, $r_t = 0.1$ mm, and $H = 25$ mm. The finite element simulation is conducted using Abaqus. The fibers are modeled by the 3D two-node thin beam element (B31). Nodes are placed in the transverse

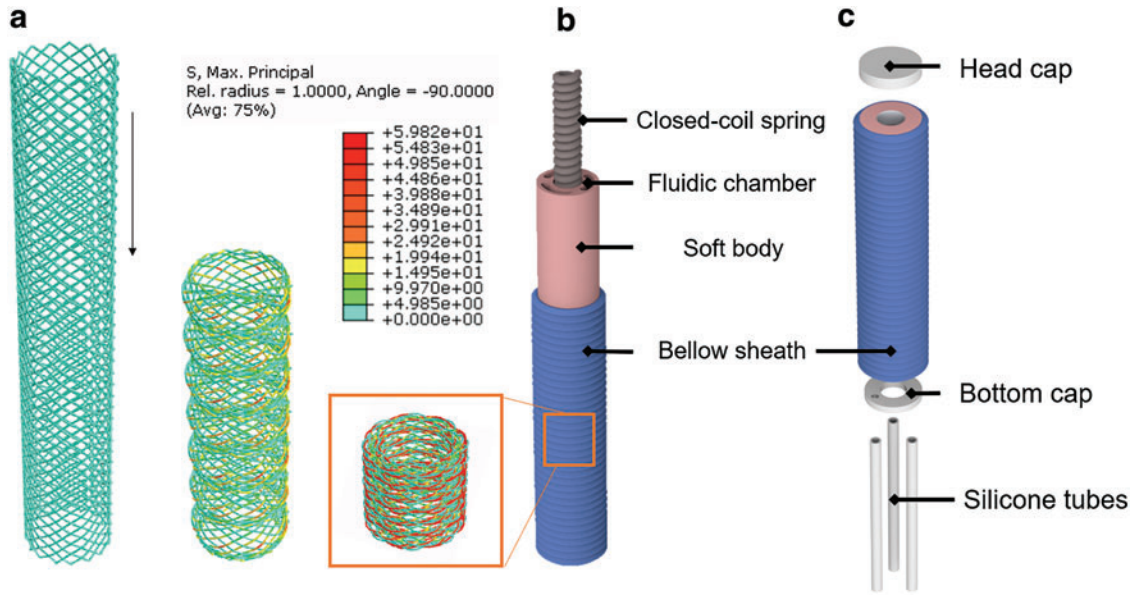


FIG. 3. (a) FEA of a braided tube being compressed into a bellow sheath. The warmer the color the higher principal stress induced. Through FEA, the complex buckling behavior of the bellow sheath could be observed. (b) Exploded view of the closed-coil spring backbone, soft body, and bellow sheath. The combined effect of these components allows much higher actuation pressures without rupture or bulging, while also enhancing the actuator's stiffness with the closed-coil spring. (c) Assembly of the SRA. Two rigid 3D-printed caps are glued to both ends to connect silicone tubes and to seal and reinforce the typically weak end connections of soft actuators. 3D, three-dimensional; FEA, finite element analysis. Color images are available online.

planes where the thread-to-thread contact occurs. The general contact option (edge-to-edge contact) is selected to handle the contact. To avoid buckling instability during the axial compression of the tube, radial inward and outward perturbing node forces are applied to promote the formation of the ripple patterns observed in the compressed tube. Figure 3a and Supplementary Video S1 show the computed result for a braided tube with initial length around 60 mm under axial compression.

Modeling of springs. To investigate the bending behavior of the spring reinforced actuators (SRAs), analytical modeling of the closed-coil spring was also pursued. The bending behavior of closed-coil springs is rarely studied since there is additional interaction between each pair of adjacent coils due to the precompression force. Initially, derivation of the open-coil spring model was undertaken before extending the formulation to the closed-coil spring. Therefore, we derive an analytical model for closed-coil springs by first separately

TABLE 1. NOMENCLATURE FOR BRAIDED TUBE GENERATION IN FINITE ELEMENT ANALYSIS AND CLOSED-COIL SPRING MODELING

Symbol	Description	Units
R_o	Mean radius of braided tube	m
r_t	Radius of braided tube thread	m
α_{top}	Initial length of the braided tube	m
H	Helical pitch of braided tube threads	m
M_{ref}	Moment acting on an open coil spring	Nm
R	Spring radius	m
R	Spring wire radius	m
E	Young modulus	$\text{kg} \cdot \text{m}^{-1} \cdot \text{s}^{-2}$
G	Shear modulus	$\text{kg} \cdot \text{m}^{-1} \cdot \text{s}^{-2}$
I	Second moment of area	m^4
J	Polar moment of area	m^4
θ_b	Inclination change per spring coil for open coil spring	rad
δ_b	Axial contraction per coil due to M_{ref}	m
δ_t	Deflection per coil due to axial force for closed-coil spring	m
F	Axial extension force acting on a closed-coil spring	N
M	Moment acting on a closed-coil spring	Nm
θ_s	Inclination changes per coil for closed-coil spring	rad
κ	Curvature of the bending closed-coil spring	m^{-1}

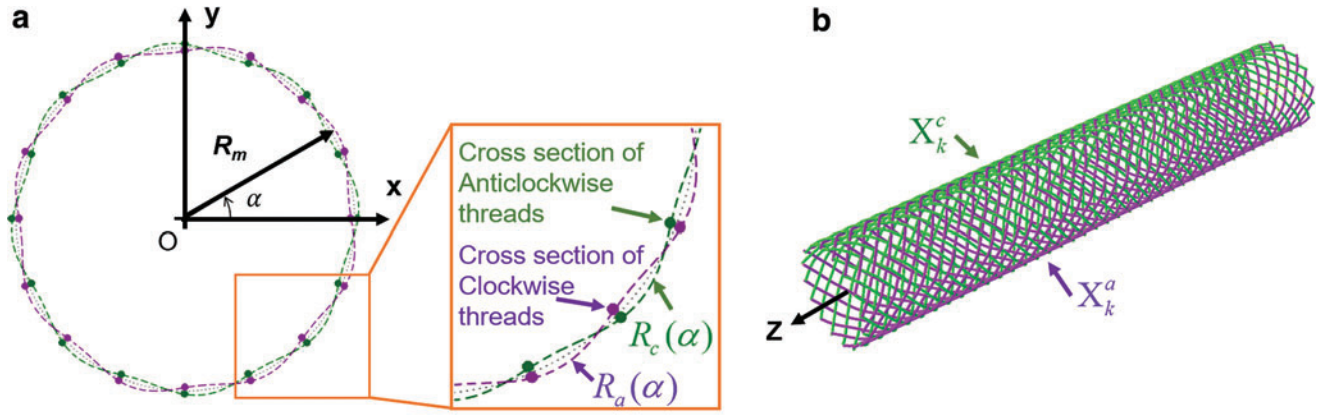


FIG. 4. Modeling procedure of the braided tube. **(a)** Transverse 2D plane of the model used to generate the braided threads and properly reconstruct the thread-to-thread contact that occurs during interweaving. *Dots in green and purple, respectively, denote the cross sections of clockwise and anticlockwise running thread in the viewed transverse plane. The dotted lines indicate the curved path taken by the threads projected to the viewed plane. The paths are generated by Equation (1) around a circle. The green and purple lines illustrate the clockwise and anticlockwise directions, respectively.* **(b)** Braided tube model generated from Equation (2) using FEA showing 32 threads interweaving clockwise (in green) and anticlockwise (in purple) along the z -axis in 3D. The fibers are modeled as 3D two-node thin beam elements (B31). 2D, two-dimensional. Color images are available online.

considering an open-coil spring that is subjected to bending. Then, we consider the axial force acting on a closed-coil spring to characterize the effect of the precompression force. Finally, by combining the two models, a bending model for a closed-coil spring is found.

Transverse moment on an open-coil spring. In the absence of precompression and coil-to-coil contact, the inclination changes of an open-coil spring subjected to moment, M_{ref} (Fig. 5a) can be considered by a quarter coil subject to a moment at its end.⁴² After resolving the moment acting on the cross section of the springs, the inclination change per spring coil, θ_b , due to M_{ref} is given as:

$$\theta_b = \int_0^{2\pi} \left(\frac{RM_{ref}}{EI} \cos^2 \phi + \frac{RM_{ref}}{GJ} \sin^2 \phi \right) d\phi \quad (3)$$

$$\theta_b = \pi RM_{ref} \left(\frac{1}{EI} + \frac{1}{GJ} \right) \quad (4)$$

where R is the spring radius, E is the young modulus, G is the shear modulus; $I = \pi r^4/4$, $J = 2I$, and r are the second moment of area, polar moment of area, and radius of the spring wire, respectively. The inclination change θ_b is illustrated in Figure 5a. Thus, the axial contraction along BB' per coil due to M_{ref} is:

$$\delta_b = R\theta_b = \pi R^2 M_{ref} \left(\frac{1}{EI} + \frac{1}{GJ} \right) \quad (5)$$

Axial force acting on a closed-coil spring. To derive the analytical model for a closed-coil helical spring subjected to axial extension force F along the centerline of the spring CC' , the small helical angle is again neglected and the coils are taken to be perpendicular to the axial force. A half-turn of a

coil twisted by the torque FR induced by F as shown in Figure 5c is considered. The right hand cross-section twists through an angle θ_t with respect to the other. From the theory of torsion, θ_t and the deflection per half-turn of coil, δ'_t , due to F are:

$$\theta_t = \frac{Fr \cdot \pi r}{GJ} \quad (6)$$

$$\delta'_t = R \cdot \theta_t = \frac{\pi Fr^3}{GJ} \quad (7)$$

Thus, the deflection per coil, δ_t , due to F is:

$$\delta_t = \frac{2\pi Fr^3}{GJ} \quad (8)$$

Transverse moment on a closed-coil spring. Considering a closed-coil spring subjected to a moment M as shown in Figure 5d, the incompressible bottom BB' of the spring will be the neutral axis along which the axial strain vanishes. Let F_c be the contact force between adjacent coils at BB' and F_p be the precompression force. With respect to CC' , the axial force and the moment can be resolved as shown in Figure 5e. As the coils are practically incompressible, the axial deflection of the closed-coil springs along BB' can be taken to be zero, that is,

$$0 = \delta_t - \delta_b \quad (9)$$

$$\pi r^2 (M - F_c R) \left(\frac{1}{EI} + \frac{1}{GJ} \right) = \frac{2\pi (F_c - F_p) R^3}{GJ} \quad (10)$$

$$F_c = \frac{2EI(F_p R) + M(EI + GJ)}{R(3EI + GJ)} \quad (11)$$

FIG. 5. Diagrams for modeling the closed-coil spring. This problem is decomposed by separately considering bending of an open coil spring and tension of a closed-coil spring. **(a)** Open coil spring subjected to a bending force. Moment, M_{ref} , acting on an open coil spring (side cross-section view), causes horizontal deflection, $\delta_b = R\theta_b$. **(b), c)** Closed-coil spring subjected to extension force inducing horizontal deflection, $\delta_t = 2\delta_t' = R\theta_t$. **(d)** Closed-coil spring subjected to moment, M , with bending axis along its side. **(e)** Resolved spring subjected to moment, M , with bending axis at its *middle*. The horizontal deflection at the *bottom* of closed-coil spring is zero as a result. Color images are available online.

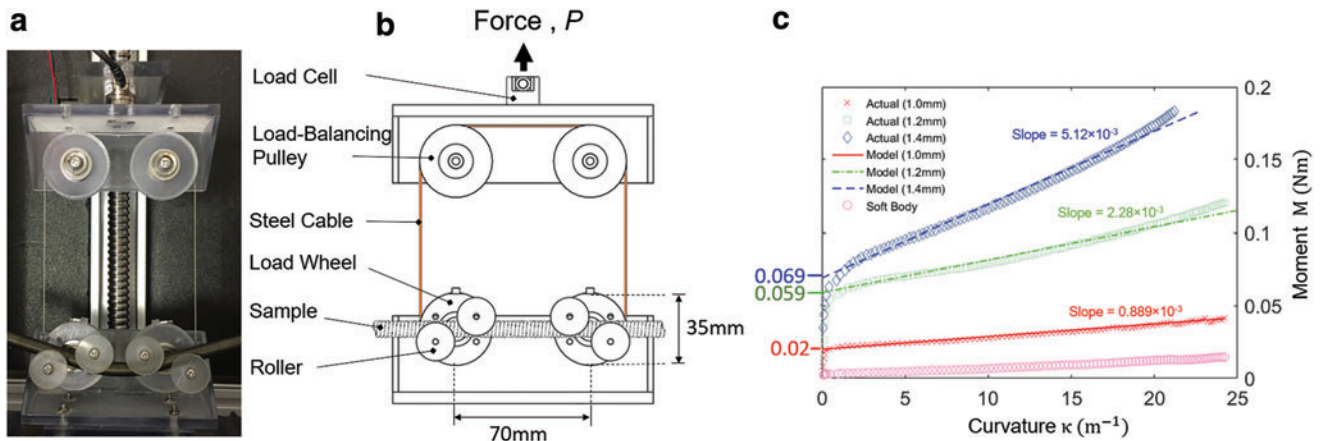
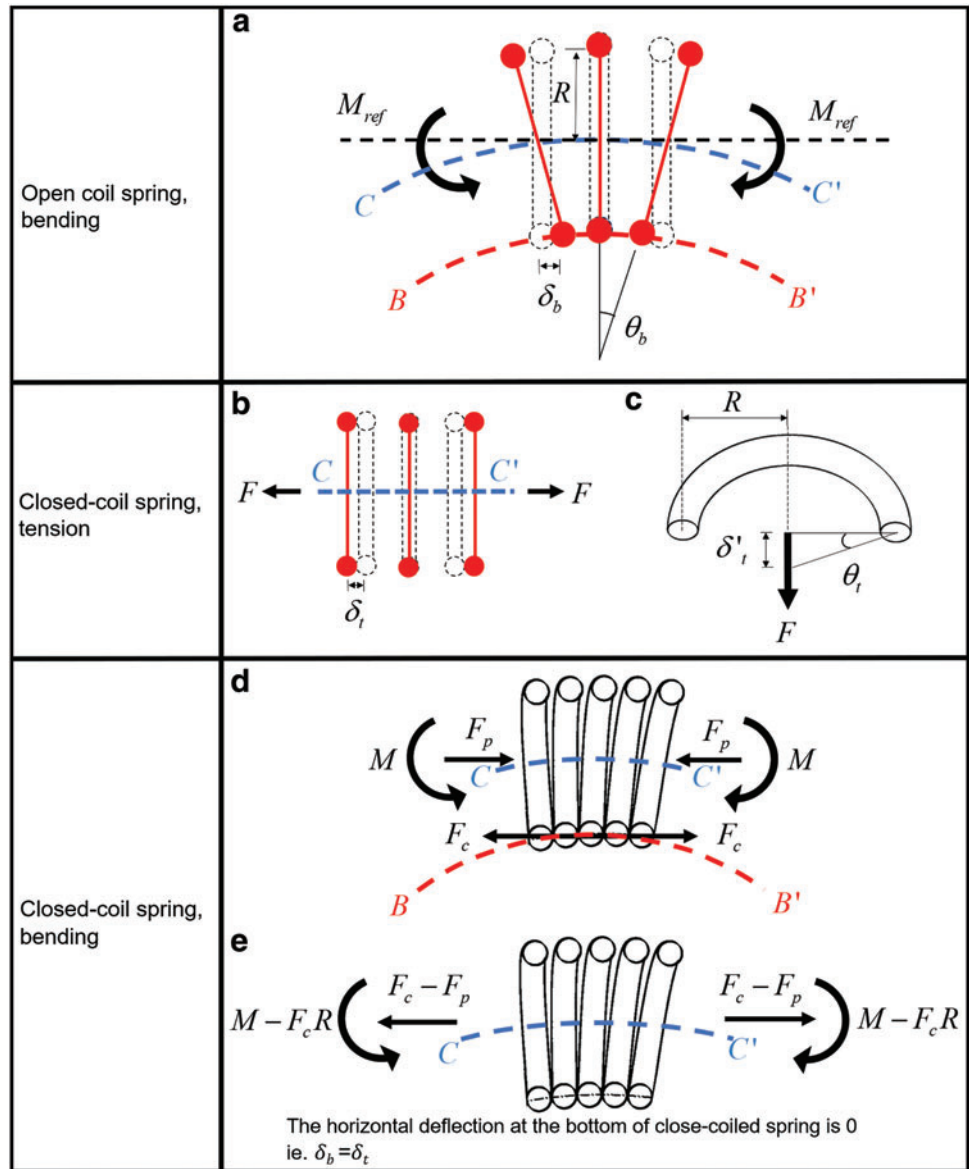


FIG. 6. **(a)** Four-point bending experiment setup for the closed coil spring. **(b)** Simplified schematics illustrating the test setup. A force, P , is applied by a linear actuator to pull two load balancing pulleys, ensuring that only a pure bending moment acts on the spring through the load wheels. **(c)** The results (markers) for the springs agree with the model prediction (lines) with different coil diameters. The y-intercepts of each curve indicate the amount of pretension in the closed-coil spring. The model-predicted bending stiffness (slope) of each spring is labeled above each corresponding line. Color images are available online.

Meanwhile, the coil opening at the noncontact side is found to be:

$$\delta_s = \delta_t + \delta_b \quad (12)$$

$$\delta_s = \frac{4\pi(GJ + EI)(-F_p R + M)R^2}{(3EI + GJ)GJ} \quad (13)$$

The inclination changes per coil due to the moment M are as follows:

$$\theta_s = \frac{\delta_s}{2R} \quad (14)$$

$$\theta_s = \frac{2\pi(GJ + EI)(-F_p R + M)R}{(3EI + GJ)GJ} \quad (15)$$

The bending curvature of the spring can then be calculated as follows:

$$\kappa = \frac{\theta_s}{2r} \quad (16)$$

Experimental setup for validation of spring model

The performance of the closed-coil springs subjected to a transverse moment is rarely mentioned in product specifications. To validate the developed model, bending tests on closed-coil springs were carried out. The traditional four-point bending test for beams is limited to small deflection. By taking reference from a previous study on measuring large deformation in super-elastic shape memory alloy tubes,^{43,44} a tailor-made and enlarged spring bending platform was built to obtain the bending moment versus curvature for the closed-coil springs.

Figure 6a shows the setup of the platform. It consists of two parts with the sample mounting at the bottom and the loading frame mounting at the top. The sample mounting contains two load wheels with diameter, D_w (35 mm), press-fitted with radial ball bearings, allowing free rotation with diameter of the steel cable, D_c (0.6 mm). Two pairs of rollers constitute the four loading points and were press-fitted with self-lubricating bushings onto the loading wheels. Lubrication was applied on the rollers to ensure free sliding of the spring sample. The load frame was attached to a high precision force sensor (Nano17; ATI Industrial Automation) that consists of a load balancing pulley with a steel cable wrapped around it. The two ends of the steel cable were separately attached to two loading wheels.

Upon driving of the leadscrew, the load-balancing pulleys were lifted upward to impart a moment to the spring sample. The force sensor could measure the load P for raising the pulleys and $P/2$ is the cable tension. Thus, the moment applied to the tube was $P(D_w + D_c)/4$. The leadscrew was driven slowly to ensure consistent recording of data throughout the test.

Modeling validation of closed-coil springs

To evaluate the proposed closed-coil spring model, several physical parameters (i.e., spring wire diameter, springs outer

diameter, and materials) of the springs can be varied to demonstrate their effect on the curvature under moment. However, to test the effect of the spring backbone on a single soft actuator, the outer spring diameter and spring material were kept unchanged. In this study, three closed-coil springs with different spring wire diameters, 1.0, 1.2, and 1.4 mm, were chosen for experimental validation. For comparison, testing of the soft body itself (without outer constraining sheath or inner reinforcement) was also performed and plotted.

The precompression force of each spring was measured by simple tensile loading, and the bending test was then carried out on the four-point bending platform. The moment imparted to the spring versus the spring bending curvature was obtained and shown for each spring wire diameter (Fig. 6c). The moment and curvature correspond to the symbols M and κ that were introduced in the modeling section (Transverse Moment on a Closed-Coil Spring section). The actual curvature of the spring was found based on the configuration of the bending setup. The predicted bending moment of the spring based on the proposed model is plotted in a dashed line. The results show a bilinear relationship for the springs upon bending and there was an obvious y-interception.

The bending stiffness of the springs and soft body was experimentally found by the slope of linear regression. The estimated bending stiffnesses for the springs were calculated to be $0.841 \times 10^{-3} \text{ Nm}^2$, $2.34 \times 10^{-3} \text{ Nm}^2$, and $5.14 \times 10^{-3} \text{ Nm}^2$ for the 1.0, 1.2, and 1.4 mm spring, respectively. The corresponding model-derived bending stiffness (slope) calculated for each spring is shown in Figure 6c. The model values are in close agreement with the experimental results, at $0.889 \times 10^{-3} \text{ Nm}^2$, $2.28 \times 10^{-3} \text{ Nm}^2$, and $5.12 \times 10^{-3} \text{ Nm}^2$ for 1.0, 1.2, and 1.4 mm, respectively. Comparatively, the estimated bending stiffness of the soft body was $0.491 \times 10^{-3} \text{ Nm}^2$.

The results indicate that an increase in precompression force increased the required torque to initiate bending, (i.e., y-interception of the graph), and the increase in spring wire diameter has a quartic relationship with the bending stiffness. The slight mismatch between the model and experimental results at the end of the spring tests may be caused by the large deformation angle under which the assumption of a closely wound coil does not hold. The bending result for the soft body shows a y-intercept close to 0, which highlights the lack of restoring force in the soft body, and also the low bending stiffness relative to the springs.

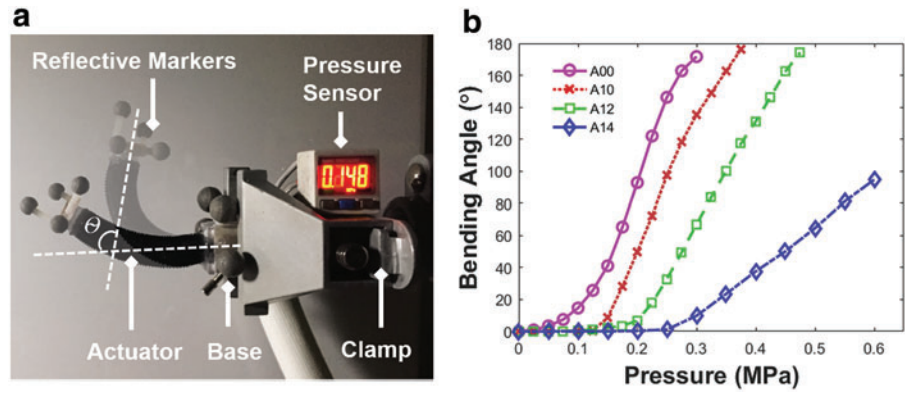
By testing the behavior of the springs before fabrication, we could provide a guideline for varying the initial spring precompression and bending stiffness before designing the actuator.

Experiments, Results, and Discussion

Experimental setup for bending tests

To evaluate the bending performance of the actuator, a tailor-made testing platform was built as shown in Figure 7a. Actuators A00, A10, A12, and A14 were fabricated. A00 contains $\phi 7$ mm polyurethane tube acting as the “backboneless” sample. A10, A12, and A14 are reinforced with spring backbones of 1.0, 1.2, and 1.4 mm spring wire diameters, respectively, while the outer diameter of the spring is 7 mm. During individual testing, each actuator was clamped as a cantilever and mounted with groups of reflective tracking

FIG. 7. (a) Bending test setup of the actuator mounted with reflective markers at its tip and tail for optical tracking of bending angle θ . Data from the pressure sensor were monitored by computer. (b) Bending angle versus pressure graph for three different spring coil diameters and with no spring (A00). It shows a bilinear relationship, with bending starting at a pressure offset (along the x -axis). As the spring coil diameter increased, the offset for bending also increased, with a similar relationship observed in Figure 6c. Color images are available online.



markers at the tip and mounted end. Digital pressure regulators adjusted the air pressure inside the chambers of the actuator, allowing it to bend. Four 3D tracking cameras at 200-fps (Vicon Vantage) tracked the actuator's 3D position and orientation based on the relative motion of the two groups of tracking markers. Data from the cameras were streamed to a computer and synced with the signal obtained from the pressure regulators.

Bending angle experiments

To understand the behavior of the actuator and validate our prediction model, the bending angle versus inflation pressure for the different spring wire diameters was tested. The actuator pressure was increased at 0.05 MPa increments until a bending angle of 180° or a chamber pressure of 0.6 MPa was reached for preventing self-contact or bursting, respectively.

The results of the experiment are shown in Figure 7b. For the spring-reinforced actuators, there was an observed bilinear relationship between the bending angle and inflation

pressure. This means that the actuator did not bend until a threshold inflation pressure was reached. This threshold inflation pressure increased proportionally with the pre-compression force of the reinforced springs, with initial bending occurring at 0.12, 0.15, and 0.2 MPa for A10, A12, and A14, respectively.

In contrast, the relationship between bending angle and pressure for the spring-less soft actuator was observed to be nonlinear, particularly at low inflation pressures. As the spring stiffness increased, the gradient of bending angle versus inflation pressure decreased. This correlates with our findings, which showed that an increase in spring wire diameter (and hence, stiffness) required a greater moment for the same bending deformation. A consequence of this relationship is that the maximum bending angle achievable by the SRA can be limited by the flexural rigidity of the spring. An example of this can be seen in A14 in which the stiffest spring is used. At the maximum allowable inflation pressure 0.6 MPa, the bending angle only reached around 100°. The bilinear relationship of the SRA curves is also seen in the moment versus curvature tests of the springs in Figure 6c.

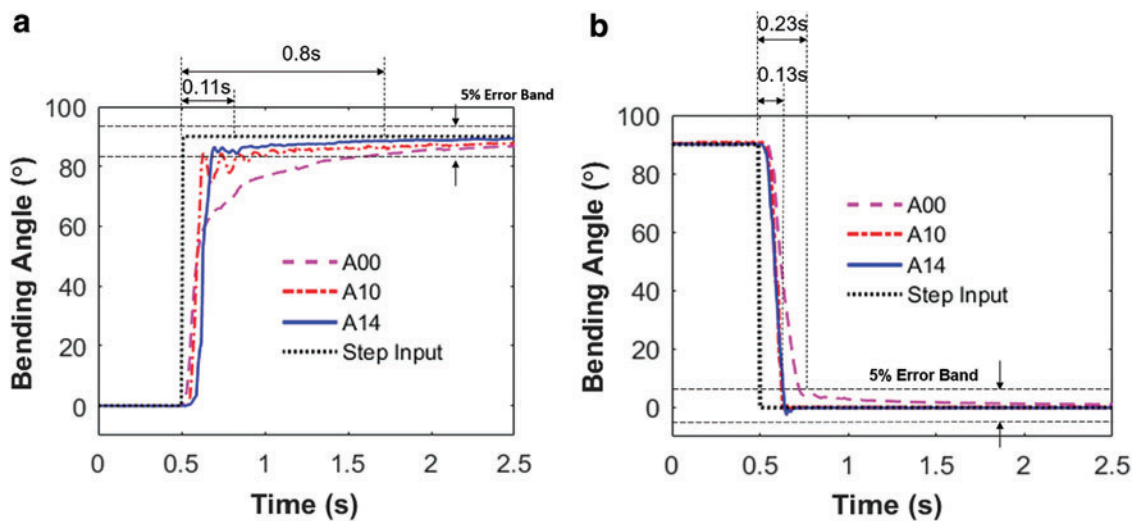


FIG. 8. Step responses of two SRAs with different wire diameters, as well as one springless actuator. (a) Step up response from 0° to 90° bending angle at 500 ms. For SRAs, the 90% rise time and settling time of the SRAs was shortened up to 80%. (b) Step-down response of actuators. Similarly, the SRAs in general showed a faster dynamic response. Color images are available online.

TABLE 2. SUMMARY OF STEP RESPONSE RESULTS

Actuator	Step-up				Step-down			
	90% Rise time (s)	Percentage of time %	5% Settling time (s)	Percentage of time %	90% Fall time (s)	Percentage of time %	5% Settling time (s)	Percentage of time %
A00	0.8	100	1.5	100	0.23	100	0.33	100
A10	0.11	13.75	0.75	50	0.135	58.6	0.145	43.9
A14	0.15	18.75	0.18	12	0.13	56.5	0.140	42.4

Generally, the addition of the spring backbone linearized the bending behavior of the actuator and the bending angle reduced with increased spring stiffness. The linearized behavior introduced by the spring could improve the controllability of the actuator.

Response to step input

One of the essential aspects of an actuator is its dynamic performance in response to desired inputs. Dynamic performance of the proposed actuator is first studied through a step response test. A00, A10, and A14 were tested. Using the testing platform in the previous section, a step-up input signal was sent at 0.5 s causing the actuator to bend from 0° to 90°. The motion capture system recorded the relative position of the actuator tip to the mounted base of the actuator. The step-up and step-down response is shown in Figure 8a. The parameters and data obtained are listed in Table 2.

The step response for the springless actuator A00 highlights the underdamping seen in typical soft robots. The actuator required a much longer time to reach the desired set point. The soft actuator had a 90% rise time of 0.8 s and a settling time within the 5% error band of 1.5 s. The inclusion of the spring backbone significantly enhanced the dynamic performance of the actuator, with an 86% lower rise time at 0.11 s, and a settling time of one-fifth of the soft actuator at 0.3 s.

A similar trend is seen in the step-down response plot from 90° to 0° for the spring-reinforced actuators. The decay time was reduced by almost half from 0.23 to 0.13 s. These im-

provements can be explained by the antagonistic restoring force provided by the spring. The actuator is able to return to the zero position quickly through the passive interaction of the actuator body and the spring.

In addition, the figure shows that the dynamic performance of the actuators can be tuned by varying the spring's wire diameter. For the step-up response, A10 with a less-stiff spring allows a steeper rise-up slope at the beginning, however, at the expense of larger amplitude oscillation near the set point. We could also observe a delayed initial response time with increased spring stiffness, correlating with the threshold inflation pressures found in Figure 8b, which indicated a higher minimum pressure to induce bending.

Bode plot

The frequency response of the actuators A00, A10, and A14 is shown in Figure 9. The actuators were commanded to bend repeatedly from 0° to 60° with 45 g tip loading with configuration as shown in Figure 9a.

The bode plot in Figure 9b highlights the improved results for the actuators with spring reinforcement. The cutoff frequency of the actuator was increased from 3 to 5 Hz after the integration of the 1.0 mm closed-coil spring and was further increased to 6 Hz with the 1.4 mm spring. The poor underdamping behavior of the soft actuator A00 may be due to the soft material body, which is slow to exhaust the air during deflation. With the presence of a stiffer spring backbone, there is an additional restoring force that helps to exhaust air in the chambers and reduce the damping effect of the air. These results indicate that the proposed SRA is able to

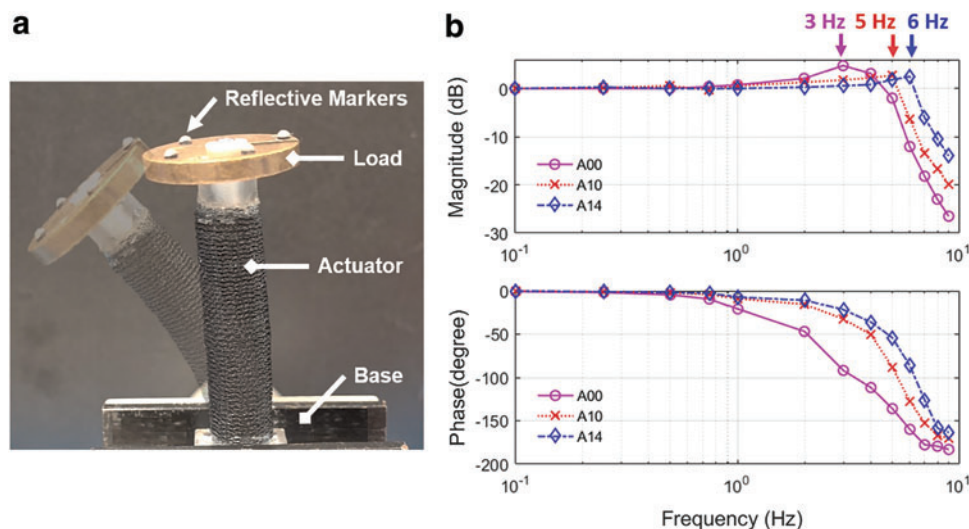


FIG. 9. (a) Bode plot setup with 45 g tip load and reflective markers for high-speed tracking. (b) Experimental bode plot of springless actuator and reinforced actuator from 0.1 to 9 Hz. The SRAs can operate at a higher cutoff frequency than the springless actuator, increasing it from 3 to 6 Hz. Color images are available online.

achieve higher operational frequencies compared to the soft actuator, which can benefit in applications where fast actuation responses are necessary.

Evaluation of actuator stiffness

To understand the effect of the springs on the SRAs, three stiffness tests were carried out. For all tests, the reaction force of the actuators was measured by an ATI Nano 17 force/torque sensor mounted on a linear actuator. The linear actuator provided a horizontal displacement in each test configuration and was limited to a 10 mm stroke at rate 1 mm/s, to maintain contact with the actuators. Similar to the step input experiment, three actuators were tested: A00, A10, and A14.

The three testing scenarios were considered. In Scenario 1, the actuator was fixed vertically downwards, and the chambers were not pressurized. A lateral force was applied to the tip by a linear actuator. In Scenario 2, the actuator was pressurized to form a 90° bending shape, and a force per-

pendicular to the bending plane was applied to the actuator tip. In Scenario 3, the actuator was pressurized to form a 90° bending shape and a force was applied to the top face of the actuator, opposing the direction of bending. For scenarios 2 and 3, the actuation pressures for introducing the 90° bending shape were 0.18, 0.22, and 0.55 MPa for A00, A10, and A14, respectively. The corresponding actuator reaction force versus tip displacement can be seen in Figure 10. Data from the F/T sensor and the corresponding displacement of the linear rail were recorded at 1 kHz.

In scenario 1, the springless actuator A00 provided a maximum resistive force of 0.5 N. In comparison, A10 demonstrated a force increase of 96% to 0.98 N and A14 increased the force by 420% to 2.7 N. In Figure 10a, a highly nonlinear relationship between force and displacement was seen for A14 (in blue). The nonlinear shape is explained by the mismatch between the tested displacement direction and the natural bending characteristic of the closed-coil spring. Shown in Figure 6, the relationship between bending moment and curvature of the springs is linear, but in this scenario, the

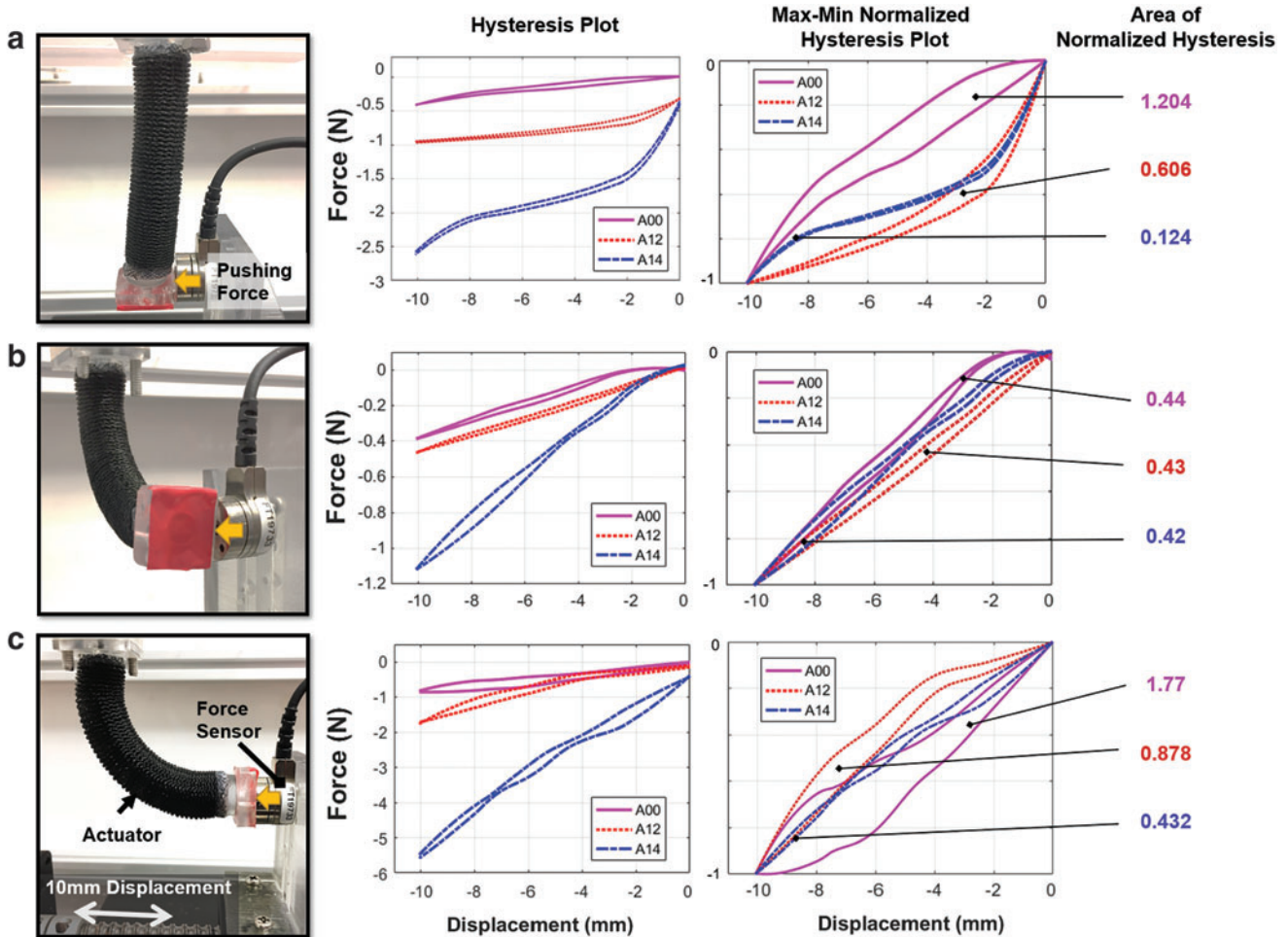


FIG. 10. Stiffness tests to study the actuator's behavior in three scenarios. An ATI Nano17 Force/Torque sensor was mounted on a linear sliding mechanism, and forces are recorded while displacing the actuator's tip by 10 mm at each posture. A force-displacement graph and a min-max normalized force-displacement graph are then plotted. (a) Actuator fixed vertically downwards with a force applied laterally to the tip. (b) Actuator pressurized to form a 90° bending shape with a force applied laterally to the tip. (c) Actuator pressurized at 90° bending shape with a force applied to the top axial face of the actuator. Color images are available online.

force is acting horizontally rather than along the bending direction.

In scenarios 2 and 3 the maximum increase in stiffness produced by A14 was 195% and 450% of the soft actuator A00, respectively. In contrast to granular jamming mechanisms, the improved stiffness of the SRAs does not come at the expense of posture recovery.

In all scenarios, the two SRAs exhibited a nonzero force at 0 mm displacement, with the exception of A10 in scenario 2. This force offset can be attributed to the pretension of the closed-coil springs. For the actuator to bend from its neutral position or along its bending plane, the pre-compression of the spring must be overcome, which is shown in Figure 10 as a force offset. The y -intercepts of the four-point bending experiment results in Figure 6c also demonstrate this similar behavior. This precompression provides a passively antagonistic mechanism that improves overall dynamic performance. In general, by integrating a closed-coil spring into the completely soft actuators, the stiffness of the system was significantly increased, without modifying its bending shape.

In this experiment, the required forces to attain the same displacement for actuators with different stiffness are also different. To appropriately compare the hysteresis of dif-

ferent actuators, we normalize the hysteresis with respect to the maximum and minimum forces applied (right column of Fig. 10). For scenario 1, the normalized hysteresis of the typical soft actuator was reduced to $\sim 10\%$ of the original hysteresis with A14. For scenario 3, the normalized hysteresis of the soft actuator A00 was reduced to 50% and 25% with A10 and A14, respectively. In scenario 2, the normalized hysteresis of the actuator was maintained at a similar level in A00, with slight improvement with the addition of spring backbones (3% and 5% for A10 and A14, respectively).

In scenario 2, only a small improvement to hysteresis is seen. This can be attributed to the forcing direction, which was acting perpendicular to the robot's bending plane. In this state, the force required to bend the actuator is very low because the spring is essentially being twisted rather than bent, which means that the precompression of the closed-coil spring could be avoided. This low force is reflected in the y -value magnitudes in the non-normalized hysteresis plot of Figure 10b. Generally, the results show that by incorporating the spring backbones, the hysteresis of a SRA decreased as the wire diameter increased, with less hysteresis when the forcing direction acts against the precompression of the springs.

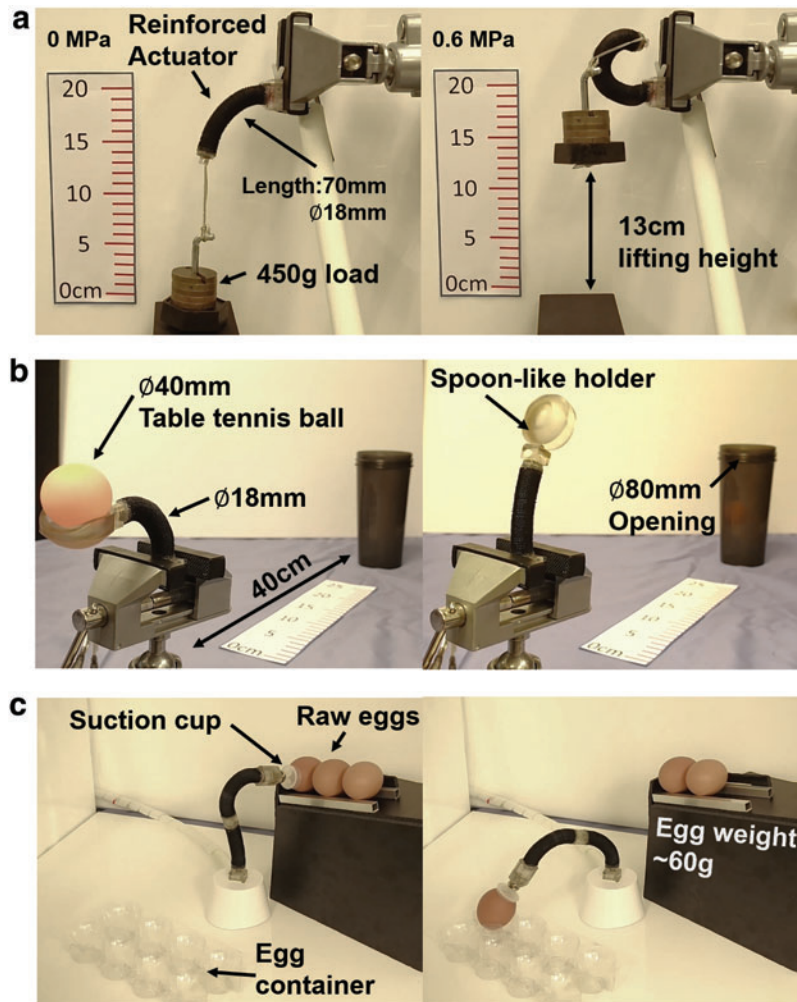


FIG. 11. (a) Weight lifting test setup to demonstrate the high lifting force of the SRA, which is capable of lifting a 450 g load (37.5 times of its weight). (b) Ball throwing test setup to demonstrate rapid motion and high repeatability of the actuator. A spoon-like holder is installed at the tip of actuator to throw a table tennis ball into a bottle. (c) Egg pick-and-place setup to demonstrate its capacity to manipulate delicate and heavy objects. Two SRAs are connected in series to form a two-segment robot arm. The arm is equipped with a suction cup at its tip and is able to pick raw eggs and place them in the egg container. See Supplementary Video S2. Color images are available online.

Manipulation tasks

Weight lifting and manipulation with tip load. To test the force output of the SRA, a 450 g load was hung at the tip of the SRA. The actuator was clamped as a cantilever and connected to a pneumatic supply with pressure regulation. With a single chamber pressurized to 0.6 MPa, the reinforced actuator could successfully lift the load as shown in movie. In contrast, the soft actuator was not able to lift the object with the same applied pressure.

The two actuators were then tested in a simple task. Both soft and reinforced actuators were programmed to move along a preplanned path with a 90 g tip loading. For each actuator, one of the channels was inflated and deflated to swing the load within 0–60°. The SRA was able to move steadily without significant overshoot or oscillation, whereas the soft actuator exhibited significant overshoot and failed to respond consistently to the input pressure signals. Moreover, upon deflation, the soft actuator was unable to return to the at-rest position. The demonstration is shown in Supplementary Video S2 and Figure 11a.

Ball throwing. To demonstrate the repeatability of the actuator, a single segment of SRA was used to repeatedly throw a table tennis ball into a target bucket located 40 cm away from the actuator. The actuator tip was attached with a spoon-like holder to hold the ball. The actuator was pressurized to bend $\sim 90^\circ$, and the balls were loaded manually before each throw. To throw the ball, the pressurized air was vented from the actuated chamber, and the actuator was allowed to return to its rest position. The demonstration shows

the actuator successfully throwing three balls consecutively into the target bucket, as shown in Supplementary Video S2 and Figure 11b.

Egg pick-and-place. To illustrate the balance between compliance and stiffness, an egg manipulation task is carried out. A two-segment manipulator equipped with a suction cup was fabricated to transfer eggs to a storage place as shown in Figure 11c. Three raw eggs with weight around 60 g are placed on an inclined plane. The manipulator was programmed with predefined actuation pressures and suction commands under open-loop to handle the eggs. Each trajectory taken was different due to the different final positions of each egg. The varied trajectories also aided in demonstrating the omnidirectional and flexible bending of the actuator. Although collisions between eggs could be seen in the video, the eggs did not break due to the retained compliance of the manipulator even after spring reinforcement.

Lateral-vertical locomotion. Previously, locomotion in soft robotics often relied on slow and rhythmic movement like those seen in peristaltic worm-like robots or by gradual crawling by legged soft robots. The improved force output and dynamic response of the proposed SRA present an opportunity for enhanced locomotion of soft robots (Fig. 12). In this demonstration, a two-segment actuator had one suction cup attached to each end. Actuation channels of the actuator and suction cup were passed through the center of springs to the pressure regulators and a suction pump. The two-segment actuator was programmed in a predefined pathway to move

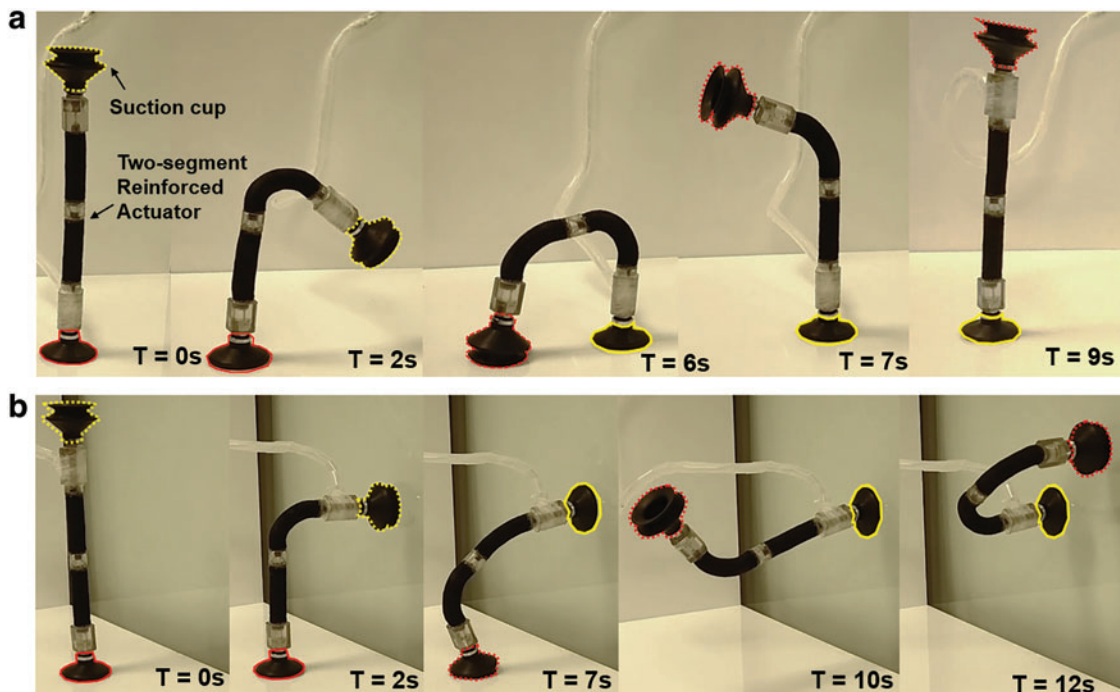


FIG. 12. (a) Time-stamped snapshots of a two-segment SRA robot equipped with two suction cups at both ends (outlined in red and yellow), which can perform lateral locomotion. It is achieved by bending of the actuator and switching of suction cups. *Solid lines* denote suction turned ON while *dash line* denotes that is OFF. (b) Time-stamped snapshots of two-segment SRA performing vertical locomotion. Although the robot is slender with a high length to width ratio (10:1), it can lift its own weight and climb a vertical surface. See Supplementary Video S2. Color images are available online.

along a flat surface and transition to a vertical surface through a movement cycle. Locomotion was performed by alternating the suction of two anchoring suction cups while bending the actuators. The motion is shown with a sequence of video frames. The figure shows the locomotion process of the two-segment actuator moving laterally (Fig. 12a) with an average speed of 40 mm/s and climbing vertically with an average speed of 15 mm/s (Fig. 12b). As seen from the video, the actuator was able to lift its own weight even with a relatively thin body cross section in thanks to the spring reinforcement. The height to width ratio of the filmed actuators is 13.5:1. The demonstration is shown in the Supplementary Video S2.

Conclusion and Future Work

Present soft fluidic actuators bring to the table compliant morphology, robustness, and passive adaptability to unknown environments. However, this comes at the cost of force output and the manipulator's dynamic response. In this study, we proposed to integrate a closed-coil spring into a soft manipulator to improve those characteristics, while retaining the omnidirectional bending ability of the original manipulator and its material compliance.

To understand the impact of the spring reinforcement on the manipulator, we developed an analytical model for closed-coil springs and performed validation with a number of spring geometries. Close correlation was found between the modeled bending behavior and the physical experimentation. This is also the first attempt to perform detailed FEA of the strain-stress behavior of the constraining braided bellow sheath. In this analysis, the braided interweaving threads, together with the complex thread-to-thread contact, were modeled.

After integrating the closed-coil spring and bellow sheath, the proposed manipulator demonstrated substantial stiffness increases up to 450% over the multiple experiment scenarios. While other stiffening approaches like granular jamming affect the bending behavior of the original manipulator and do not allow active bending, the closed-coil spring still allowed natural bending of the original soft manipulator, although a higher pressure was required to reach the same bending angles.

Experiments for step response and frequency response were also performed, which generally highlighted significant improvements to the overall dynamic response of the spring-reinforced system. The proposed manipulator was also implemented in a number of demanding applications such as locomotion and pick-and-place procedures to demonstrate the improved performance, which can be seen in Supplementary Video S2. In general, the spring-reinforced actuator provided enhanced performance in most measures compared to the purely soft actuator.

In our future work, we aim to further characterize the effect of spring integration by also considering the soft robot material characteristics. This will include modeling of the complex interaction among the spring backbone, soft robot body, and constraining bellow sheath. We will also aim to implement reconfigurability of the robot, by allowing simple swapping of the spring based on the desired application, and also investigate the impact of changing different spring parameters on overall performance.

Author Disclosure Statement

No competing financial interests exist.

Funding Information

This work is supported, in part, by the Croucher Foundation, the Research Grants Council (RGC) of Hong Kong (17202317, 17227616, and 27209515) and Innovation and Technology Commission of Hong Kong (UIM/353), the National Research Foundation of Korea Grant (NRF-2016R1A5A1938472), and the Natural Science Foundation of China (U1613202).

Supplementary Material

Supplementary Video S1
Supplementary Video S2

References

1. McMahan W, Chitrakaran V, Csencsits M, *et al.* Field trials and testing of the OctArm continuum manipulator. In Proceedings 2006 IEEE International Conference on Robotics and Automation (ICRA), Orlando, FL. IEEE, 2006.
2. Kier WM, Smith KK. Tongues, tentacles and trunks: The biomechanics of movement in muscular-hydrostats. *Zool J Linnean Soc* 1985;83:307–324.
3. Suzumori K, Iikura S, Tanaka H. Development of flexible microactuator and its applications to robotic mechanisms. In Proceedings 1991 IEEE International Conference on Robotics and Automation (ICRA), Sacramento, CA. IEEE, 1991.
4. Trivedi D, Rahn CD, Kier WM, *et al.* Soft robotics: Biological inspiration, state of the art, and future research. *Appl Bionics Biomech* 2008;5:99–117.
5. Suzumori K. Elastic materials producing compliant robots. *Robot Auton Syst* 1996;18:135–140.
6. Lee K-H, Fu DK, Leong MC, *et al.* Nonparametric online learning control for soft continuum robot: An enabling technique for effective endoscopic navigation. *Soft Robot* 2017;4:324–337.
7. Tsukagoshi H, Kitagawa A, Segawa M. Active hose: An artificial elephant's nose with maneuverability for rescue operation. In Proceedings 2001 IEEE International Conference on Robotics and Automation (ICRA), Seoul, Korea. IEEE, 2001.
8. Robertson MA, Paik J. New soft robots really suck: Vacuum-powered systems empower diverse capabilities. *Sci Robot* 2017;2:eaan6357.
9. Connolly F, Walsh CJ, Bertoldi K. Automatic design of fiber-reinforced soft actuators for trajectory matching. *Proc Natl Acad Sci U S A* 2017;114:51–56.
10. Seok S, Onal CD, Wood R, *et al.* Peristaltic locomotion with antagonistic actuators in soft robotics. In Proceedings 2010 IEEE International Conference on Robotics and Automation (ICRA), Anchorage, AK. IEEE, 2010.
11. Shepherd RF, Ilievski F, Choi W, *et al.* Multigait soft robot. *Proc Natl Acad Sci U S A* 2011;108:20400–20403.
12. Connolly F, Polygerinos P, Walsh CJ, *et al.* Mechanical programming of soft actuators by varying fiber angle. *Soft Robot* 2015;2:26–32.
13. Stokes AA, Shepherd RF, Morin SA, *et al.* A hybrid combining hard and soft robots. *Soft Robot* 2014;1:70–74.
14. Bicchi A, Tonietti G. Fast and “soft-arm” tactics [robot arm design]. *IEEE Robot Autom Mag* 2004;11:22–33.
15. Yao L, Niiyama R, Ou J, *et al.* PneuUI: Pneumatically actuated soft composite materials for shape changing interfaces. In Proceedings of the 26th Annual ACM Symposium on User Interface Software and Technology, Scotland, UK. ACM, 2013.

16. Polygerinos P, Wang Z, Galloway KC, *et al.* Soft robotic glove for combined assistance and at-home rehabilitation. *Robot Auton Syst* 2015;73:135–143.
17. Doumit M, Fahim A, Munro M. Analytical modeling and experimental validation of the braided pneumatic muscle. *IEEE Transact Robot* 2009;25:1282–1291.
18. Ilievski F, Mazzeo AD, Shepherd RF, *et al.* Soft robotics for chemists. *Angew Chem* 2011;123:1930–1935.
19. Cianchetti M, Ranzani T, Gerboni G, *et al.* Soft robotics technologies to address shortcomings in today's minimally invasive surgery: The STIFF-FLOP approach. *Soft Robot* 2014;1:122–131.
20. Steltz E, Mozeika A, Rembisz J, *et al.* Jamming as an enabling technology for soft robotics. In *Electroactive Polymer Actuators and Devices (EAPAD) 2010*, San Diego, CA. International Society for Optics and Photonics, 2010.
21. Jiang A, Ataollahi A, Althoefer K, *et al.* A variable stiffness joint by granular jamming. In *ASME 2012 International Design Engineering Technical Conferences and Computers and Information in Engineering Conference*, Chicago, IL. American Society of Mechanical Engineers, 2012.
22. Ranzani T, Gerboni G, Cianchetti M, *et al.* A bioinspired soft manipulator for minimally invasive surgery. *Bioinspir Biomim* 2015;10:035008.
23. Qi P, Qiu C, Liu H, *et al.* A novel continuum manipulator design using serially connected double-layer planar springs. *IEEE/ASME Transact Mechatron* 2016;21:1281–1292.
24. Santiago JLC, Godage IS, Gonthina P, *et al.* Soft robots and kangaroo tails: Modulating compliance in continuum structures through mechanical layer jamming. *Soft Robot* 2016;3:54–63.
25. Wall V, Deimel R, Brock O. Selective stiffening of soft actuators based on jamming. In *Proceedings 2015 IEEE International Conference on Robotics and Automation (ICRA)*, Seattle, WA. IEEE, 2015.
26. Chen Y, Le S, Tan QC, *et al.* A reconfigurable hybrid actuator with rigid and soft components. In *Proceedings 2017 IEEE International Conference on Robotics and Automation (ICRA)*, Singapore. IEEE, 2017.
27. Nemiroski A, Shevchenko YY, Stokes AA, *et al.* Arthro-bots. *Soft Robot* 2017;4:183–190.
28. Natividad RF, Del Rosario MR, Chen PC, *et al.* A hybrid plastic-fabric soft bending actuator with reconfigurable bending profiles. In *Proceedings 2017 IEEE International Conference on Robotics and Automation (ICRA)*, Singapore. IEEE, 2017.
29. Heung KH, Tong RK, Lau AT, *et al.* Robotic glove with soft-elastic composite actuators for assisting activities of daily living. *Soft Robot* 2019;6:289–304.
30. Marchese AD, Onal CD, Rus D. Autonomous soft robotic fish capable of escape maneuvers using fluidic elastomer actuators. *Soft Robot* 2014;1:75–87.
31. Seok S, Onal CD, Cho K-J, *et al.* Meshworm: A peristaltic soft robot with antagonistic nickel titanium coil actuators. *IEEE/ASME Transact Mechatron* 2013;18:1485–1497.
32. Aschenbeck KS, Kern NI, Bachmann RJ, *et al.* Design of a quadruped robot driven by air muscles. In *Proceedings of the First IEEE/RAS-EMBS International Conference on Biomedical Robotics and Biomechanics, BioRob 2006*, Pisa, Italy. IEEE, 2006.
33. Shin D, Yeh X, Khatib O. Variable radius pulley design methodology for pneumatic artificial muscle-based antagonistic actuation systems. In *Proceedings 2011 IEEE/RSJ International Conference on Intelligent Robots and Systems (IROS)*, San Francisco, CA. IEEE, 2011.
34. Hogan N. Adaptive control of mechanical impedance by coactivation of antagonist muscles. *IEEE Transact Autom Control* 1984;29:681–690.
35. Cianchetti M, Ranzani T, Gerboni G, *et al.* STIFF-FLOP surgical manipulator: Mechanical design and experimental characterization of the single module. In *Proceedings 2013 IEEE/RSJ International Conference on Intelligent Robots and Systems (IROS)*, Tokyo, Japan. IEEE, 2013.
36. Ranzani T, Cianchetti M, Gerboni G, *et al.* A soft modular manipulator for minimally invasive surgery: Design and characterization of a single module. *IEEE Transact Robot* 2016;32:187–200.
37. Laschi C, Mazzolai B, Cianchetti M. Soft robotics: Technologies and systems pushing the boundaries of robot abilities. *Sci Robot* 2016;1:eaah3690.
38. Yoon H-S, Yi B-J. A 4-DOF flexible continuum robot using a spring backbone. In *Proceedings 2009 International Conference on Mechatronics and Automation (ICMA)*, Changchun, China. IEEE, 2009.
39. Choi D-G, Yi B-J, Kim W-K. Design of a spring backbone micro endoscope. In *Proceedings 2007 IEEE/RSJ International Conference on Intelligent Robots and Systems (IROS)*, San Diego, CA. IEEE, 2007.
40. Lekakou C, Elsayed Y, Geng T, *et al.* Skins and sleeves for soft robotics: Inspiration from nature and architecture. *Adv Eng Mater* 2015;17:1180–1188.
41. Noh Y, Sareh S, Back J, *et al.* A three-axial body force sensor for flexible manipulators. In *Proceedings 2014 IEEE International Conference Robotics and Automation (ICRA)*, Hong Kong, China. IEEE, 2014.
42. Wahl AM. *Mechanical Springs*. New York, NY: Penton Publishing Company, 1944.
43. Reedlunn B, Churchill CB, Nelson EE, *et al.* Tension, compression, and bending of superelastic shape memory alloy tubes. *J Mech Phys Solids* 2014;63:506–537.
44. Bundara B, Tokuda M, Kuselj B, *et al.* Superelastic tension and bending characteristics of shape memory alloys. *Metals Mater* 2000;6:293–299.

Address correspondence to:

Ka-Wai Kwok
7/F, Haking Wong Building
Department of Mechanical Engineering
The University of Hong Kong
Pokfulam
Hong Kong
China

E-mail: kwokkw@hku.hk